

Noise focusing and the emergence of coherent activity in neuronal cultures

Javier G. Orlandi ^{*}, Jordi Soriano ^{*}, Enrique Alvarez-Lacalle [†], Sara Teller ^{*}, and Jaume Casademunt ^{*}

^{*}Departament d'ECM, Facultat de Física, Universitat de Barcelona. Martí i Franqués 1, 08028 Barcelona, Spain

[†]Departament Física Aplicada, EETAC. Universitat Politècnica de Catalunya UPC. Esteve Terrades 5, Castelldefels, Spain

Experiments

Culture preparation. Rat cortical neurons from 18–19-day-old Sprague-Dawley embryos were used in the experiments. All procedures were approved by the Ethical Committee for Animal Experimentation of the University of Barcelona. Following Refs. [1, 2], dissection was carried out in ice-cold L-15 medium enriched with 0.6% glucose and 0.5% gentamicin (Sigma-Aldrich). Embryonic cortices were isolated from the rest of the brain and neurons dissociated by gently pipetting through gradually narrower pipette tips.

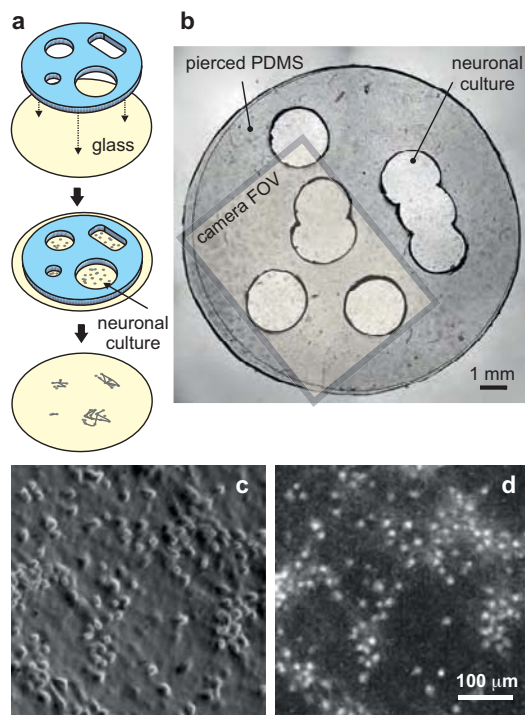


Fig. S1. Neuronal cultures. **a**, Schematic representation of the culturing process by using pierced PDMS molds (blue) attached to glass coverslips (yellow). The preparation process (top) included piercing, autoclaving and poly-L-lysine coating; the culturing process (center) yielded to the formation of mini-cultures in the pierced areas; the final process (bottom) consisted in the removal of the PDMS mold and the preparation of the culture for the measurements. **b**, Actual image of combined glass-PDMS structure 11 days after plating. The rectangular area depicts the maximum field-of-view (FOV) of the camera (8.2×6.1 mm). **c**, Bright field image of a small region of a culture. Round objects are neurons' cell bodies. **d**, Corresponding fluorescence image integrated over 200 frames. Bright spots are firing neurons.

Cortical neurons were plated on 13 mm glass coverslips (#1 Marienfeld-Superior) that contained a pierced PDMS mold, as illustrated in Fig. S1a. Prior to plating, glasses were washed in 70% nitric acid for 2 h, rinsed with double-distilled water (DDW), sonicated in ethanol and flamed. During glass cleaning, several 13 mm diameter layers of PDMS 1 mm thick were prepared and subsequently pierced with biopsy punchers (Integra-Miltex) of diameters in the range 2 – 5 mm. Each pierced PDMS mold typically contained 5 to 8 cavities, either circular or quasi-rectangular by overlapping consecutive pierced areas (Fig. S1b). The PDMS molds were then attached to the glasses and the combined structure autoclaved at 120°C, firmly adhering to one another. Each combination of glass and PDMS was placed in 15 mm diameter culture wells for neuronal plating and maintenance. To facilitate a homogeneous distribution of neurons in the cultures, the PDMS-glass structure was incubated overnight with 0.01% Poly-L-lysine (PLL, Sigma). For each dissection we prepared 24 wells, giving rise to about 100 mini-cultures of areas in the range 2–20 mm². We also prepared bigger cultures by plating the neurons directly on the 13 mm diameter glass coverslips.

Cultures were incubated at 37°C, 95% humidity, and 5% CO₂ for 4 days in plating medium [90% Eagle's MEM — supplemented with 0.6% glucose, 1% 100X glutamax (Gibco), and 20 μg/ml gentamicin— with 5% heat-inactivated horse serum, 5% heat-inactivated fetal calf serum, and 1 μl/ml B27]. The medium was next switched to changing medium [90% supplemented MEM, 9.5% heat-inactivated horse serum, and 0.5% FUdR (5-fluoro-deoxy-uridine)] for 3 days to limit glia growth, and thereafter to final medium [90% supplemented MEM and 10% heat-inactivated horse serum]. The final medium was refreshed every 3 days by replacing the entire culture well volume. Plating was carried out with a nominal density of 1 million cells/well (5000 neurons/mm²). The actual density of the neuronal culture was measured at the end of each experiment by counting the number of active neurons, and ranged between 500 and 700 neurons/mm². Fig. S1b shows an actual culture 11 days after plating. A detail of the culture depicting the neurons is shown in Figs. S1c-d. Although neurons grew both over glass and PDMS, the connectivity between the top and bottom areas was minimal. The PDMS was gently removed before measuring, and we did not detect any substantial damage in the network after PDMS removal.

Experimental setup and imaging. Neuronal activity was studied at day *in vitro* 9–18, which corresponds to a state of development sufficiently mature for the culture to show rich spontaneous activity. Prior to imaging, and after removing the PDMS mold, cultures were incubated for 40 min in External Medium (EM, consisting of 128 mM NaCl, 1 mM CaCl₂, 1 mM MgCl₂, 45 mM sucrose, 10 mM glucose, and 0.01 M HEPES; treated to pH 7.4) in the presence of the cell-permeant calcium sensitive dye Fluo-4-AM (4 μl Fluo-4 per ml of EM).

The culture was washed with fresh EM after incubation and finally placed in a recording chamber containing 4 ml of EM.

The recording chamber sits on a temperature controller stage that provided stable temperature during recording with an error of 0.1°C. The stage was mounted on a Zeiss inverted microscope equipped with a 2.5X objective and a variable optical zoom in the range 0.32X–0.81X. Neuronal activity was monitored through fluorescence calcium imaging (Fig. S1d) using a Hamamatsu Orca Flash 2.8 CMOS camera attached to the microscope. Images were acquired with a speed in the range 33.33 – 200 frames per second (fps) and a spatial resolution in the range 3.44 – 8.51 μm/pixel (depending on the optical zoom and camera settings). As described later, the recording speed was adjusted in each experiment to balance image quality, minimum photo-damage to the cells, and sufficient temporal resolution. The size of the images was automatically set by the camera to fit the requested acquisition speed. The maximum image size that we could set was 960×720 pixels (width×height), i.e. 8.2×6.1 mm² at the lowest resolution and acquisition speed (33.33 fps). At 200 fps, for instance, the maximum image size was 960×144 pixels, corresponding to 8.2×1.2 mm². The number of neurons monitored depended on the actual size of the mini-culture and the recording settings, but all experiments contained at least 1000 neurons.

Experimental procedure. Prior to recording, the mini-cultures were carefully inspected to reject those with dead cells or poor distribution of neurons. The selected culture was next placed in the recording chamber and oriented respect to the camera to fit as many cultures as possible in the field of view, as illustrated in Fig. S1b. An example of spontaneous activity measurements in mini-cultures is shown in the accompanying movie *activity-cultures.avi*.

In all experiments we monitored the spontaneous activity of the neuronal network, and at a temperature of 25°C unless stated otherwise. Experiments were carried out in two steps. In the first step we recorded a short image sequence at 100 fps for about 5 min, and containing a few bursts. The data was then pre-analyzed to determine the typical propagation speed of the front. The camera settings were then readjusted to set the maximum image size and recording quality according to this speed. In our experiments we observed that a front propagating at $v \approx 10$ mm/s (Fig. 1 of the main manuscript) could be well resolved at speeds of 33.33–50 fps, while propagations at $v \approx 100$ mm/s (typically for cultures at DIV 14–27) required an acquisition speed of 200 fps. The accompanying movies *front-mini.avi* and *front-big.avi* show, respectively, illustrative examples of front propagation in a mini-culture and in a 13 mm glass coverslip.

The second step corresponded to the actual recording of spontaneous activity. We acquired a long sequence of typically 45 min in duration that contained several network bursts, on the order of 100. A second recording of 45–60 min long was also programmed for those experiments in which the neuronal network was manipulated, e.g. to study inhibition or different temperatures. Cultures under continuous recording are healthy for about 2–3 h, and therefore we limited the experiments to 1.5 h to prevent artifacts in the data due to culture deterioration.

We designed the experiments to explore different culture sizes, the excitatory–inhibitory balance, temperature, as well as the influence of physical damage to the network. The experiments are summarized in Fig. S3.

As indicated, experiments carried out at day *in vitro* (DIV) 9–18 showed rich and sustained spontaneous activity. This activity took the form of bursts. However, for complete-

ness, we also tested (see Fig. S3): a) very young cultures at DIV 5–6, which lack inhibition but do fire [2]; b) maturing cultures at DIV 7–8, characterized by a low activity and low propagating velocity; and c) relatively old cultures at DIV 20–27, which are highly active but that may exhibit a more complex bursting dynamics [3]. Data averaging was carried out only with cultures that differed a maximum of 2 days for DIV < 9, or 3 days for DIV ≥ 9. Although nucleation and front propagation could be observed in all cases, the dynamics of the front depended on culture age, culture size, and the balance between excitation and inhibition.

Pharmacology. Sufficiently mature neuronal cultures (above DIV 6–7) contain both excitatory and inhibitory neurons. To study the influence of the inhibitory sub-network in the initiation and propagation of the activity front, data was first recorded with both excitatory and inhibitory connections active (E+I networks). Next, the culture was treated with 40 μM bicuculline methiodide (Sigma), a GABA_A receptor antagonist, to completely block inhibition, and the activity of the excitatory-only culture (E network) was measured again. Bicuculline was applied to the culture 5 min before the actual recording of activity for the drug to take effect.

Data analysis. The recorded image sequences were processed at the end of the experiment to retrieve the fluorescence intensity of 1000–3000 individual neurons as a function of time. To reconstruct the neurons' ignition sequence, we first isolated a particular bursting event from the rest of the sequence (see, e.g. movie *front-mini.avi*). Next, for the fluorescence signal of each neuron, we carried out two linear fits: one fit of the data points preceding the firing and another one of the points encompassing the fast increase in fluorescence (Fig. S2a). The crossing point of the two lines provided the ignition time of the neuron. This process was repeated for all neurons, and the final activation times data set was ordered to reconstruct the neurons' firing sequence (Fig. S2b). This information, together with the spatial position of the neurons, provided

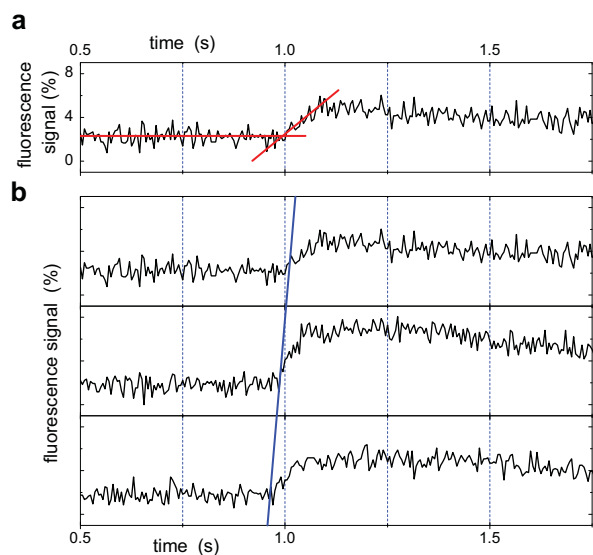


Fig. S2. Data analysis. **a**, Example of the fluorescence signal of an individual neuron, together with the linear fits used to determine the onset time of firing. **b**, Fluorescence traces of three neurons located (from top to bottom) at the left edge, center, and right edge of the region studied. The thick blue line connects the measured onset times, and illustrates the propagation of an activity front from right to left.

Culture properties			Realizations (N)	Experimental condition	Recording time DT [min]	Observed bursts in DT (n)	Dynamics		Comments
Type	Area [mm ²]	DIV					<IBI> [s]	<v> [mm/s]	
Circ, 2 mm	3.0	10	2	E+I	45	38	83 (96)	3 (1)	Standard experiments on pierced PDMS molds [small size]
				E	45	14	173 (122)	6 (1)	
Circ, 2 mm	2.0	9	2	E+I	30	45	47 (64)	3 (1)	
				E	60	9	360 (208)	6 (1)	
Circ, 3 mm	7.1	5	2	E+I	30	29	62 (23)	3 (1)	Standard experiments on pierced PDMS molds [medium size]
				E	45	(no activity)	-	-	
Circ, 3 mm	7.1	6	2	E+I	40	45	51 (32)	10 (3)	
				E	45	3 (erratic)	-	3 (2)	
Circ, 3 mm	7.1	8	2	E+I	25	111	13 (7)	6 (2)	
				E	45	3 (erratic)	-	9 (2)	
Circ, 3 mm	7.1	9	1	E+I	25	52	23 (11)	13 (2)	
				E	45	3 (erratic)	-	28 (4)	
Circ, 3 mm	6.9	9	5	E+I	45	98	26 (19)	8 (2)	
				E	60	44	78 (114)	16 (3)	
Circ, 3 mm	5.6	10	1	E+I	30	58	30 (23)	16 (5)	
				E	45	5 (erratic)	-	28 (3)	
Circ, 3 mm	5.2	10	1	E+I	45	101	26 (16)	11 (2)	
				E	45	7 (erratic)	270 (72)	24 (3)	
Circ, 3 mm	6.2	10	4	E+I	45	63	44 (46)	20 (5)	
				E	60	21	156 (81)	28 (7)	
Circ, 4 mm	7.4	11	2	E+I	40	68	35 (10)	5 (1)	
				E	60	44	83 (64)	9 (1)	
Circ, 3 mm	8.1	13	2	E+I	40	49	48 (47)	13 (3)	
				E	60	13	265 (172)	21 (5)	
Circ, 3 mm	6.9	12	2	E+I normal	35	24	75 (46)	13 (2)	Cutting experiments
				E+I after cut	35	58	37 (24)	10 (2)	
Circ, 3 mm	7.3	12	2	E+I normal	35	56	31 (24)	12 (3)	
				E+I after cut	45	60	43 (43)	11 (2)	
Rect, 6x3 mm ²	15.8	9	1	E+I	40	134	17 (8)	16 (3)	Standard experiments on pierced PDMS molds [big size]
				E	60	60	53 (36)	18 (3)	
Rect, 6x4 mm ²	16.8	9	2	E+I	40	157	15 (8)	12 (2)	
				E	60	42	79 (62)	16 (2)	
Rect, 7x3 mm	16.9	11	3	E+I	40	148	16 (8)	6 (2)	
				E	60	92	39 (24)	9 (2)	
Rect, 6x3 mm ²	13.8	15	2	E+I	35	34	56 (33)	18 (4)	
				E	55	28	117 (108)	26 (4)	
Rect, 5x3 mm ²	7.3	16 – 18	6	E+I [25 °C]	40	43	96 (32)	13 (3)	Temperature experiments
				E+I [37 °C]	40	34	108 (41)	14 (2)	
				E [25 °C]	40	17	165 (29)	20 (6)	
				E [37 °C]	40	16	180 (43)	22 (7)	
			1	E [49 °C]	40	2	-	33 (10)	
13 mm glass	132.7	5	2	E+I	30	38	47 (25)	19 (6)	Standard experiments on 13 mm cover glasses
				E	60	(no activity)	-	-	
13 mm glass	132.7	6	2	E+I	25	81	18 (9)	13 (3)	
				E	45	14 (erratic)	185 (114)	11 (3)	
13 mm glass	132.7	9	3	E+I	20	96	11 (10)	6 (1)	
				E	20	14	13 (9)	26 (3)	
13 mm glass	132.7	12	3	E+I	30	92	19 (23)	13 (2)	
				E	45	19	144 (102)	23 (4)	
13 mm glass	132.7	13	3	E+I	25	64	24 (15)	15 (2)	
				E	45	62	44 (37)	51 (5)	
13 mm glass	132.7	14	3	E+I	30	179	10 (3)	9 (3)	
				E	60	122	29 (19)	13 (2)	
13 mm glass	132.7	15	2	E+I	35	219	9 (4)	17 (3)	
				E	50	91	33 (8)	34 (6)	
13 mm glass	132.7	16	2	E+I	40	72	33 (21)	18 (3)	
				E	45	35	79 (29)	26 (3)	
13 mm glass	132.7	27	2	E+I	35	264	8 (6)	26 (5)	
				E	55	169	19 (6)	43 (6)	
13 mm glass	132.7	20	3	E only	90	152	36 (29)	73 (5)	
13 mm glass	132.7	21	4	E only	90	163	32 (13)	108 (8)	
13 mm glass	132.7	8	2	E+I (before cut)	20	56	21 (10)	23 (5)	Cutting experiment
				E+I (after cut)	20	18 (erratic)	62 (41)	22 (7)	

Fig. S3. Summary of the experiments. 'DIV' is culture days *in vitro*. Cultures were always grown on cover glasses, and the presence of PDMS pierced molds during culture development provided mini-cultures of either circular or rectangular shapes. 'Type' indicates then the nominal size and shape of the circular or rectangular PDMS pierced molds. For those experiments without PDMS, the diameter of the cover glass is provided instead. 'Area' is the actual region covered by the neurons in the mini-culture, measured at the end of the experiment. The 'standard experiments' correspond to measures with excitation and inhibition active (E+I networks), followed by measurements in the same culture with inhibition blocked upon application of 40 μ M bicuculline (E networks). Some special experiments were inspired by the model, and included the removal of a part of the network (cutting experiments) and the exploration of different temperatures. The number in brackets beside the measurements of inter-burst interval (IBI) and average velocity of the propagating front $\langle v \rangle$ is the standard deviation of the data. IBIs and standard deviations are not computed for those experiments with 5 or less bursts.

the map of neuronal activation shown in Fig. 1 of the main manuscript (see also Fig. S5). The first group of neurons to

fire determined the position of the nucleation point, i.e. the

center of burst initiation. Since the burst propagates as a circular wave, the velocity of the front was calculated as the average radial displacement at different time intervals.

The reconstruction of the neurons' ignition sequence was slightly sensitive to the signal-to-noise ratio, i.e. fluorescence signal quality, and on the parameters of the linear fits, i.e. the fitting origin and range. To determine the coordinates of the nucleation point and their associated error, we took advantage of the fact that activity propagates as a circular wave, and proceeded as follows. For each activity front, we first calculated the average position of initiation for the first N firing neurons, with $N = 1, 2, 3, 5$ and 10 , and took the standard deviation of these positions as the error ε_{xy} in the location of the nucleation site. This initial calculation was carried out using preset fitting parameters, which were later refined to take those that minimized ε_{xy} . The propagation velocity of the front is measured along consecutive radius, centered at the nucleation site and separated by $200 \mu\text{m}$.

Nucleation probability density. Each spontaneous activity measurement provided a set of about 50 – 200 nucleation points and associated errors. The number of bursts depended on culture properties, e.g. maturation or size, and network connectivity, e.g. inhibition active or blocked. The corresponding nucleation probability distribution of these nucleation points was calculated as follows. First, we coarse-grained the area of the neuronal culture by applying a grid with a lateral size $s = 10 \mu\text{m}$. This grid was next associated to a matrix initiated with zeros. For each nucleation point, we added 1 at the matrix element with indexes (i, j) that corresponded to the coordinates (x, y) of the nucleation point. The matrix elements at concentric radius from the nucleation point, and up to the error ε_{xy} , were added with radially decreasing values according to a Gaussian distribution. In this way we computed the spatial distribution of nucleation sites weighted by their errors. The matrix was finally normalized and divided by the coarse-graining factor s^2 (in mm^{-2}) to obtain the probability density plotted in the manuscript. A comparison of the distribution of burst initiation points and the final nucleation probability function is shown in Fig. S4.

Experimental Lorenz curves. These curves show the cumulated probability of nucleation as a function of their covered area in the culture. Lorenz curves therefore provide a visual

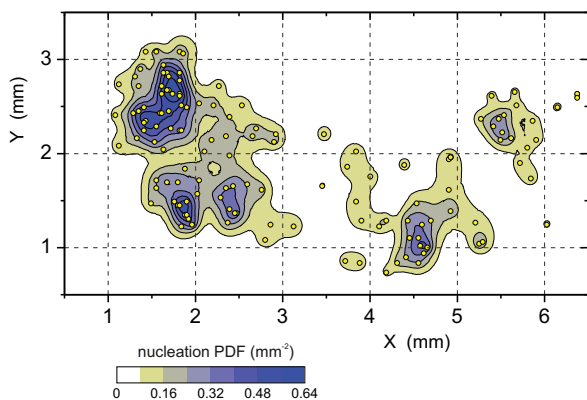


Fig. S4. Nucleation probability function for the experiment shown in Fig. 2b of the main manuscript together with the corresponding burst initiation points (yellow dots). Nucleation probability is obtained by coarse-graining the 134 nucleation points with an algorithm that includes the error in their detection. The data shown corresponds to a measurement with both excitation and inhibition active, and at DIV 9.

aid for the observed small area coverage of nucleation sites. Homogeneously distributed nucleation sites across the culture would result in a straight line along the diagonal of the plots shown in Fig. 2c since each area unit of the culture would contribute equally to nucleation. Hence, deviations from this line mark the tendency for nucleation to occur in a relatively small area of the culture, as observed both in experiments and simulations.

The Lorenz curves shown in Fig. 2c of the main manuscript were obtained from the probability density of nucleation sites, as follows. We considered the normalized, cross-grained matrix of nucleation sites and ordered its values p_i in a descending order. Next, we plotted the cumulated sum $\sum_i^n p_i$ as a function of i/n , with n the total number of elements in the matrix.

Big cultures. Fig. S5 provides an example of activity propagation in a large, 13 mm diameter culture, studied at DIV 21. Big cultures have the advantage that spontaneous activity is richer and more periodic (Fig. S5a). Additionally, the entire field of view contains neurons in these experiments (Figs. S5b-c, accompanying movie `front-big.avi`) and therefore burst initiation and front propagation can be better resolved (Figs. S5d-e). The major disadvantage of big cultures in our setup is that initiation occurs both in the monitored field of view and the regions outside. The statistics of nucleation sites is therefore partial. For this reason we have not used big cultures for the study of the nucleation sites distribution.

Additional experiments

We also carried out a series of experiments that were inspired by the theory. They provide direct evidences of the sensitivity of the nucleation process on both network architecture and background neuronal activity. The experiments strengthen the validity of the theoretical framework and the *in silico* approach. We show first that changes in temperature modify the nucleation sites, hinting at the importance of noise in neuronal network dynamics. Next, we show that a modification of the architecture of the network through ablation of neurons and connections considerably changes the distribution of nucleation sites, revealing the nonlocal nature of the nucleation process and the subtle interplay between connectivity and dynamics.

Influence of temperature. The chamber in our setup that contains the neuronal culture is equipped with a temperature controller in the range 25 – 50 °C. To test temperature effects, in a typical experiment we first measured activity for 30 min at 25 °C in a culture with both excitation and inhibition active (E+I network), then switched to 37 °C, and measured again for another 30 min. We next blocked inhibition with 40 μM bicuculline (E network) and repeated the measurements at the two temperatures. In total we investigated $N = 6$ cultures with similar size (7.3 mm^2 in area), density (400 neurons/ mm^2) and maturation (*day in vitro*, DIV, 16 – 18).

In general we obtained similar results with both temperatures, with no qualitative difference in activity. Global bursts of spontaneous activity appeared at both temperatures, and with similar shapes. Nucleation points and propagation velocities could also be described well. For each experimental condition we analyzed $n = 20 - 60$ bursts, and determined the inter-burst interval (IBI) and the velocity v of the propagating front. The results are shown in Fig. S6a. Within experimental error we could not observe any difference in the overall dynamics of the network due to temperature. How-

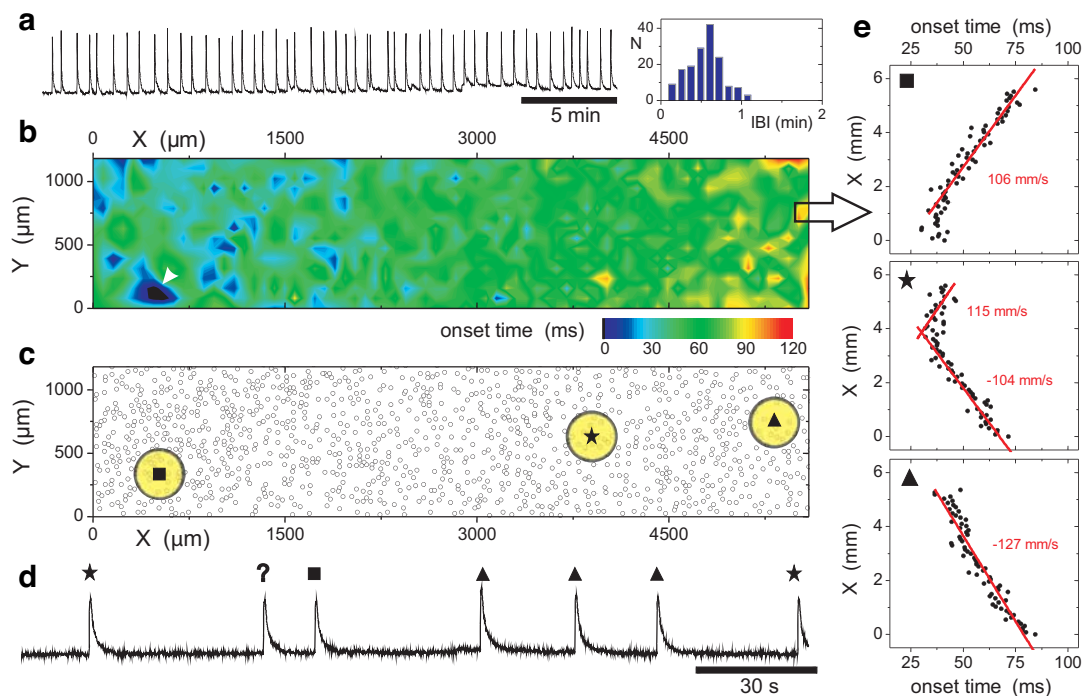


Fig. S5. Experiments on big cultures. **a**, Spontaneous activity in a neuronal network cultured on a 13 mm diameter glass coverslip, studied at DIV 21 and with only excitation active. Data corresponds to the average fluorescence signal of ~ 1000 neurons. Fluorescence peaks correspond to network bursts. The histogram shows the distribution of inter-burst intervals (IBIs) along the total 90 min duration of the recording, and provides an average bursting period of 40 s. **b** High speed (200 frames/s) monitoring of a network burst in a 5.6×1.2 mm² region of the culture. Onset times correspond to the occurrence of individual neuronal firing within the burst. Activity initiates in a small area at the bottom-left corner (white arrow) and propagates towards the right edge of the region. **c** Corresponding spatial distribution of neurons together with the three most frequent nucleation sites of the region, based on the analysis of 10 bursts. **d** Detail of a train of bursts with their associated nucleation sites. For the burst marked with "?" activity started outside the monitored region. **e** Onset times (averaged over the Y direction of the region) along X, for the three most frequent nucleation sites. The linearity of the data points reveals the advance of the activity front at a constant velocity, with its value given by the slope of the least squares fit.

ever, we did observe a significant variation in the distribution of nucleation sites, as shown in Fig. S6b for a culture with only excitatory synapses active. The foci of nucleation displaced from the top areas of the culture to its left-center areas as the temperature increased. Although temperature has a complex role in neuronal dynamics, we hypothesize that, in the context of our noise focusing model, temperature may increase the spontaneous release of neurotransmitters, therefore increasing the background activity of the network. This, in turn, may modify the frequency and structure of activity avalanches, ultimately modifying the spatial distribution of nucleation events.

Modification of network circuitry through cutting. In these experiments we studied the alteration in the spatial distribution of nucleation sites upon removal of a small region of the neuronal culture. We considered cultures with both excitatory and inhibitory synapses active (E+I network), and at DIV 12–13. E+I networks are convenient since they provide the maximum firing rate and therefore rich nucleation statistics. In a typical experiment we first measured the spontaneous activity in 3 mm diameter mini cultures for about 40 min. We next used a scalpel to cut out a small region of the culture, and measured again the spontaneous activity for another 40 min. The cut out region contained about 15–20% of the neurons of the original network. We finally computed the

distribution of nucleation sites before and after the damage. We studied $N = 4$ different cultures of equal size and nominal density. Initiation statistics is based on $n \simeq 50$ bursts per experimental condition.

The results for a particular culture are shown in Fig. S6c. Before the cut, initiation switched between two well separated nucleation sites, a big one at the top-right of the culture, and a smaller one at the bottom-left. After the cut, the small nucleation site (at the vicinity of the damaged region) disappeared, while the remaining one (located at about 1 mm from the damage) changed its spatial configuration. We note that the cut not only eliminated a number of neurons and associated background activity, but also their input and output connections, effectively remapping the flow of activity in the culture. Interestingly, the average activity of the network increased after the damage, and illustrates the subtle interplay between connectivity and activity. In the framework of the noise focusing phenomena, the spatial modification of the nucleation distribution probability has a clear interpretation: a series of avalanches that originated in the left side of the culture and that possibly ended on its right side were completely eliminated.

In silico model

Metric construction of the network. To construct the neuronal network we model pyramidal neurons as circular cell bodies

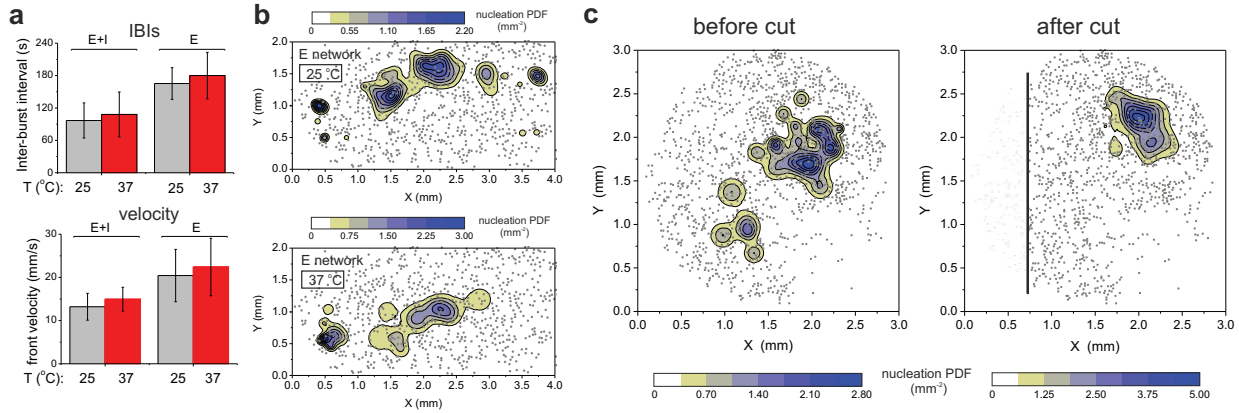


Fig. S6. Additional experiments. **a**, Comparison of the values for the inter-burst intervals (IBIs) and front velocity for cultures studied at two temperatures, 25°C and 37°C, and two connectivity conditions, E+I and E. Statistics is based on $N = 6$ cultures of 7.3 mm² in area at DIV 16 – 18, with $n = 20 - 60$ bursts analyzed for each temperature and condition. **b**, Nucleation probability distribution for a culture studied at two temperatures, 25°C and 37°C, at DIV 18 and with only excitatory synapses active. Culture size was 4 × 2 mm². Small grey-yellow circles are neurons. **c**, Comparison of the nucleation probability distribution for a 3 mm diameter culture before and after damaging the network with a sharp blade. Culture was studied at DIV 12 and had both excitatory and inhibitory synapses active. The black lines shows the position and length of the incision. Neurons are shown as a small grey-yellow circles. Neurons in the cut out region are shown in a lighter color. Nucleation statistics is based on $n = 30$ bursts before the cut, and on $n = 57$ bursts after it. Spontaneous activity recordings lasted 35 min in both cases.

(somas) with fixed diameter $\phi_s = 15 \mu\text{m}$. Somas are randomly placed on a bidimensional area described by the coordinates (x, y) , and without any overlap between cell bodies. The total number N of neurons is given by the density ρ . We consider densities in the range 250 – 1000 neurons/mm² to match the values observed experimentally.

From each soma on the substrate an axon grows in a random direction following a quasi-straight path, as described later, and with a final length that is given by a Rayleigh distribution, of the form

$$p(\ell) = \frac{\ell}{\sigma_\ell^2} \exp\left(-\frac{\ell^2}{2\sigma_\ell^2}\right), \quad [1]$$

where $\sigma_\ell^2 = 900 \mu\text{m}^2$ is the variance of the distribution and its value is chosen so that the average axonal length matches the value $\langle \ell \rangle \simeq 1.1 \text{ mm}$ measured in our experiments.

Experimental observations show that axons do not grow straight but with a fluctuating orientation. To mimic this condition realistically, we apply the following algorithm to position each axon. We initially divide the total length l into small segments $\Delta\ell = 10 \mu\text{m}$ long. The first segment is placed at the end of the neuron cell body, and with an orientation that follows a uniform angular distribution. The i -th segment is then placed at the end of the previous one, and oriented following a Gaussian distribution around the previous segment given by

$$p(\theta_i) = \frac{1}{\sqrt{2\pi\sigma_\theta^2}} \exp\left(-\frac{(\theta_i - \theta_{i-1})^2}{2\sigma_\theta^2}\right), \quad [2]$$

where θ_{i-1} is the angle between the segment $i - 1$ and the x - y plane. σ_θ is chosen to obtain a long persistence length (typically $\sigma_\theta \sim 15^\circ$). The growing process is then repeated until all segments are laid down.

To complete the description of the network we set up the dendritic tree. Based on the work by Wen et al. [4], and other similar studies, we consider the dendritic tree of a neuron as a disk of diameter ϕ_d . The diameter was drawn from a Gaussian distribution with mean $\mu = 300 \mu\text{m}$ and standard deviation of $\sigma^2 = 40 \mu\text{m}^2$

Connectivity. The growth process described above leads to a geometric construction of the network connectivity based on the following rules. First, a connection can be established only when the axon of a given neuron intersects the dendritic tree of any other neuron, as illustrated in Fig. S7. And second, those neurons that fulfill this geometric condition will connect with probability α . This probability of connection is considered to be independent of the overlapping length between the axon and the dendritic tree that is intersected [4]. For $\alpha = 1$, any axon that crosses a dendritic tree establishes a connection. In large cortical structures where the geometrical distribution is well known (e.g. the Blue Brain Project) α is in the range 0.1 – 0.2. However, in neuronal cultures α is higher due to the reduced connectivity and dimensionality. In our case we will consider α in the range 1/3–1.

The whole network connectivity that results from this geometric construction is stored in the adjacency matrix A , where $A_{ji} = 1$ identifies a connection $i \rightarrow j$.

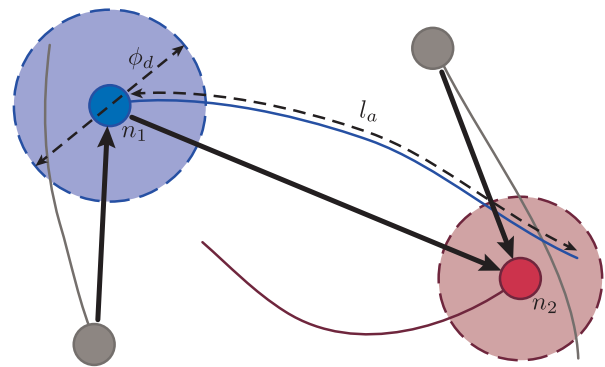


Fig. S7. Metric construction of the neuronal network. For clarity only 4 neurons are shown, indicating their somas and axons. The area covered by the dendritic tree is depicted for two neurons (blue and red circular areas). A connection between two neurons is established with a certain probability whenever the axon of a neuron crosses the dendritic tree of another one.

Soma dynamics. Following Refs. [5, 6] we describe the soma dynamics and the generation of action potentials by a quadratic integrate-and-fire model with adaptation. This description leads to a system of two coupled non-linear ordinary differential equations, of the form

$$C \frac{dv}{dt} = R_q(v - v_r)(v - v_t) - R_U U + R_s I_s + R_\eta \eta, \quad [3]$$

$$\tau_a \frac{dU}{dt} = k_b(v - v_r) - U, \quad [4]$$

$$\text{if } v \geq v_p \text{ then } v \leftarrow v_c, U \leftarrow U + \Delta U. \quad [5]$$

Eq. (3) specifies the dynamics of the soma membrane potential $v(t)$, with C the leaky capacitance. Three effective currents enter the soma: U is an inhibitory current that accounts for the internal slow currents generated by the activation of K^+ ion channels and the inactivation of the Na^+ channels; I_s is the synaptic inputs from other neurons; and η a noise term. Eq. (4) describes the dynamics of the inhibitory current. τ_a is the main time-scale of the inhibitory current, k_b its sensitivity to sub-threshold fluctuations of the membrane potential, and ΔU describes the after-spike reset of U caused by slow high-threshold Na^+ and K^+ conductances.

The quadratic part $(v - v_r)(v - v_t)$ of Eq. (3) has two fixed points, one stable, v_r , and one unstable, v_t . These points characterize the dynamics of the neuron. Insufficient stimulation keeps $v < v_t$ and the membrane potential relaxes towards its resting potential v_r . However, repeated stimulation brings v above the threshold value v_t . The potential then grows rapidly up to a preset peak value $v \geq v_p$ that is associated to the generation of a spike. The potential is thereafter reset to v_c .

In the numerical simulations we have used a reduced form of the above equations, given by

$$\tau_c \dot{v} = k(v - v_r)(v - v_t) - u + I + \eta, \quad [6]$$

$$\tau_a \dot{u} = b(v - v_r) - u, \quad [7]$$

$$\text{if } v \geq v_p \text{ then } v \leftarrow v_c, u \leftarrow u + d. \quad [8]$$

This model reproduces well the spiking behavior of most cortical neurons. Although in cortical networks several types of neurons coexist, we have restricted ourselves to regular spiking neurons. The set of parameters used to describe the dynamic behavior of the spiking neurons is listed in a table at the end of the SI.

We have tested the influence of neuronal variability in the dynamics of the network, and observed that the overall network behavior does not significantly change. For instance, we have studied the influence of subpopulations of low and high threshold spiking neurons (LTSN and HTSN, respectively). We introduced 10% of HTSN (with $v_c = -45$ mV and $d = 50$) [5] and 10% of LTSN (divided in two groups, 5% with $v_c = -40$ mV, $d = 55$, and 5% with $v_c = -35$ mV, $d = 60$), and found no significant differences.

Synaptic dynamics. Each connection between two neurons is associated to a chemical synapse with its own dynamics. For simplicity we consider that when a neuron generates an action potential, all its presynaptic terminals release neurotransmitters at the same time.

Let us consider the dynamics of a synapse that connects neuron i with neuron j ($i \rightarrow j$). When the neuron i generates a spike at time t_m it triggers the release of neurotransmitters at the synapse and induces a post-synaptic current at neuron j . This current travels from the synapse to the soma and depolarizes the membrane, facilitating an action potential at

neuron j . The total input currents on neuron j is then

$$I_j(t) = \sum_{i=1}^{k_{in}^j} \sum_{t_m < t} E_i(t, t_m), \quad [9]$$

where $E_i(t, t_m)$ is the current induced by neuron i at time t as a result of the action potential generated at time t_m . The first summation comprises all input connections k_{in}^j on neuron j , and the second one all spikes previously generated. Note that the subset t_m is in general different from neuron to neuron, and can be viewed as the spike history of neuron i .

Each of the post-synaptic currents is modeled as a sudden increase in intensity at the time of action potential t_m and an exponential decay afterwards. For our excitatory currents we consider only the effect of AMPA receptors since they are the main source of activity in network bursts. The post-synaptic currents due to the firing of neuron i can be expressed as

$$E_i(t, t_m) = g_A D_i(t_m) \exp\left(-\frac{t - t_m}{\tau_A}\right) \theta(t - t_m), \quad [10]$$

where g_A is the strength of the synapse (associated to the receptor density at the post-synaptic terminal) and τ_A the characteristic decay time of the post-synaptic current. $D(t)$ accounts for short-term depression, a mechanism in which synapses reduce their efficacy due to depletion of neurotransmitters in their presynaptic vesicles [7]. Short-term depression acts on a fast time scale and therefore affects the spontaneous bursting activity. Depression is modeled as an internal variable D that describes the efficacy of the neuron presynaptic terminals. D has a resting value of 1 and relaxes exponentially as [6, 8, 9]

$$\dot{D} = \frac{1}{\tau_D}(1 - D) - (1 - \beta)D\delta(t - t_m), \quad [11]$$

where τ_D is the characteristic recovery time associated to vesicle recycling [10, 11]. This recovery time is highly variable from culture to culture, and is the time scale that controls the inter burst intervals. It is typically in the range 0.5 – 20 s. The release of neurotransmitters at the synapse as a consequence of firing results in a reduction of D to βD , with $\beta < 1$. Subsequent action potentials before full recovery will induce post-synaptic currents, but gradually with lower strength, resulting in a reduced efficacy to generate a spike in the post-synaptic neuron.

Sources of noise. The last term of Eq. (3) accounts for the noise present in the system. We consider that the noise has two different sources. The first one is a Gaussian white noise associated to fluctuations in membrane potential. The second one is a shot noise representing the spontaneous release of neurotransmitters in the presynaptic terminals. This spontaneous release generates small currents (*minis*) in the post-synaptic terminal that travel down the dendritic tree to the soma, in the same way as evoked currents. The only difference between spontaneous and evoked currents is their amplitude. Minis play a pivotal role in cultures and are thought to be an important source of noise in them. [11, 12].

Triangles, clustering and network maps. Given the adjacency matrix of the network A , the total number of triangles for each neuron is obtained from the diagonal elements of $T_T = 1/2(A + A^T)^3$. Specific directional triangles can be identified by similar operations, for example $T_{FB} = A^3$ for feedback loops (see [13, 14] for details). Triangles are directly related to clustering, an observable that characterizes percolation properties of the network [15]. In general we observed

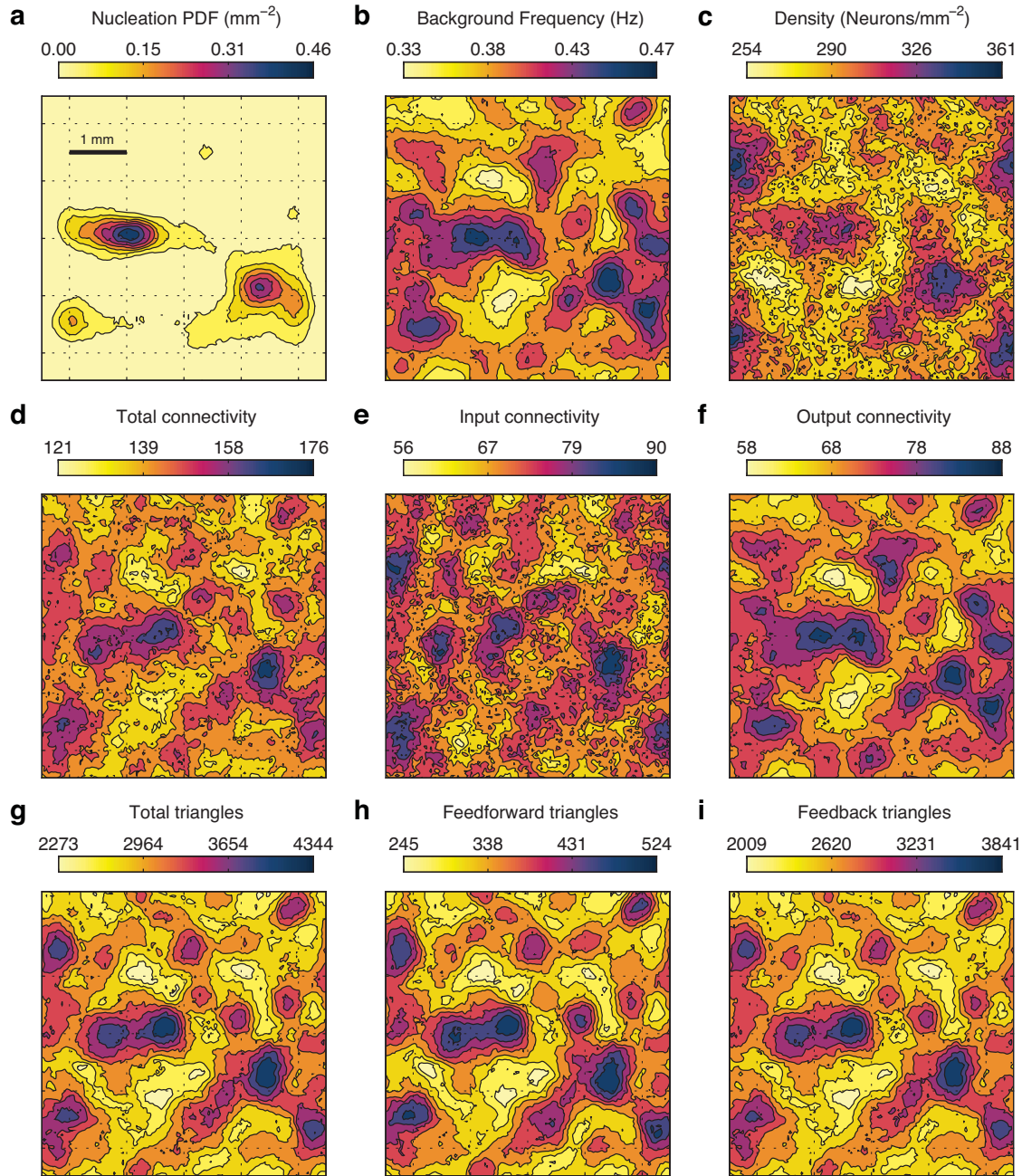


Fig. S8. Full set of network observables **a**, Nucleation probability density function for the same network shown in Fig. 5 of the main manuscript. **b**, Background frequency, i.e. average spiking activity outside the bursts. **c**, Neuronal density. Although the map appears noisy at this coarse-graining scale, the fluctuations are small, $\sim 15\%$ from the mean value. **d-f**, Network connectivity maps separated between total (input+output), input and output. **g-i**, Triangle maps separated between total (feedback + feed-forward), feed-forward and feedback triangles.

that the noise amplification mechanism described in the main manuscript is strongly favored by the total number of triangles, but not by their configuration. Specific triangle configurations may facilitate noise focusing, but in a minor degree and with a contribution that is difficult to assess. We also ob-

served that, due to the nature of the neuronal dynamics, the total number of triangles is a better predictor of activity than clustering itself, and clustering was only used when comparing networks with the same average connectivity. This relies in the fact that the strength of the connections is not scaled with the number of connections.

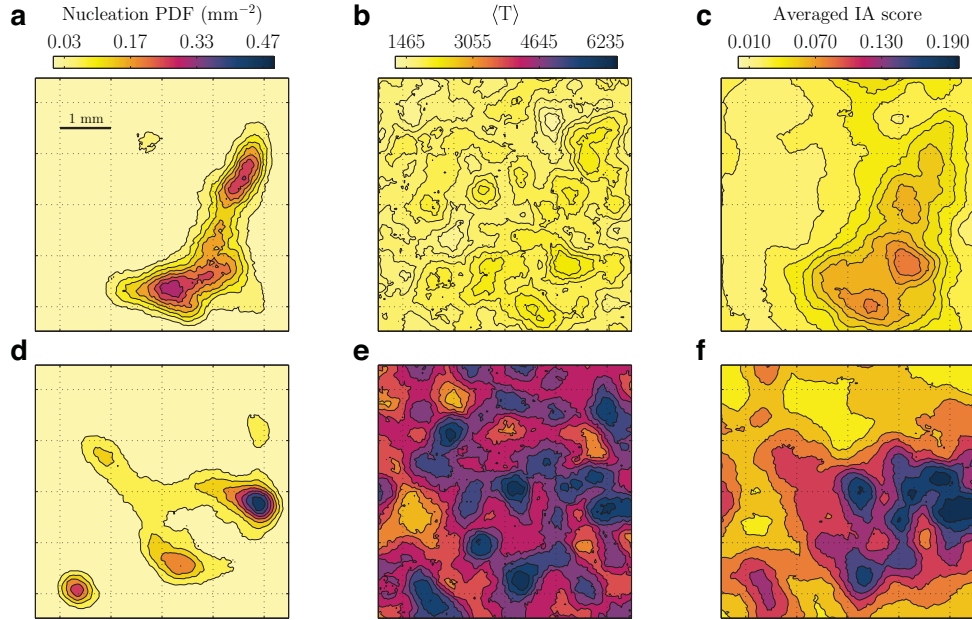


Fig. S9. Network observables and clustering Comparison of the network observables for two networks with the same dynamical parameters and connectivity $\langle k \rangle = 70$. Top row, network with low clustering, $\rho = 500$ neurons/mm², $\alpha = 0.4$. Bottom row, network with high clustering, $\rho = 200$ neurons/mm², $\alpha = 1$. The color code of each observable is the same for the two networks. **a,d**, Comparison of the nucleation probability density function. The distribution in the high clustering network is sharper, reaching a local probability of ~ 0.45 mm⁻². The highest peak in the low clustering network is ~ 0.30 mm⁻². **b,e**, Number of triangles formed by network connections per neuron. Since the average connectivity of both networks is the same, this is a direct measure of the clustering coefficient. **c,f**, averaged IA score of each neuron. The IA score is defined by the fraction of times a given neuron participates in an IA. This is also higher in the high clustering network, showing a better ability of the nucleation sites to collect the activity from their surroundings.

The properties of individual neurons, such as input and output connectivity or triangles, can be conveniently described by a coarse-grained representation, namely *network maps*. In the simulations we coarse-grained these neuronal properties over a circle with a radius given by the average connectivity correlation length ξ_c which is usually of the order of the size of the dendritic tree, i.e. $300 \mu\text{m}$. The precise value of this correlation length is extracted from the decay of the connectivity correlation function $X_c(r)$, defined as the average number of connections that each pair of neurons have in common, as a function of the distance between neurons r ,

$$X_c(r) = \sum_{i,j=1}^N \sum_{k=1}^N (A_{ik}A_{jk} + A_{ki}A_{kj}) \delta(|\vec{r}_i - \vec{r}_j| - r). \quad [12]$$

In general $X_c(r)$ can be fitted by an exponential $\sim \exp(-r/\xi_c)$ which defines the correlation length.

Avalanches and nucleation

Avalanche detection. The activity in the model presented can be best described in terms of avalanches of activity. They are observed due to the strong dynamic correlations of the whole neuronal population. To characterize them, we proceed as follows. First, we identify a neuron that has generated a spike. Next, we scan all its output neurons for the occurrence of spikes in a short time window $\sim 2\tau$, where τ is the characteristic decay time of the post-synaptic current. The process is iteratively repeated for all the newly detected spikes until no more spikes are found. When multiple avalanches with

different initiation neurons have spikes in common, they are merged into a single, bigger avalanche.

Those avalanches that die out (i.e. no more correlated spikes are found) are considered as background avalanches (BAs) of size n , with n the number of spikes involved. Instead, an avalanche that recruits over 95% of the population in a very short time window is considered an ignition avalanche (IA). This avalanche (which comprises all the activity) can then be separated in two parts: the real IA (the precursor of the burst) and the burst itself. IAs have the characteristic signature of a steep amplification of activity over time, which is not present in BAs.

Nucleation sites and clustering. As we have described in the manuscript, avalanches of activity in the network tend to focus on a set of nucleation sites. These sites act as attractors for the avalanches of a large surrounding area of the network, and ultimately lead to the initiation of a burst. The total number and the relative weight of these nucleation sites change from network to network.

In Fig. S8 we show the complete set of topological observables associated to the network shown in Fig. 5 of the main manuscript.

In Fig. S9 we show the statistics of two networks with the same dynamical parameters but with different densities ρ and probability of connection α . We choose ρ and α so that the two networks have the same connectivity degree $\langle k \rangle \propto \rho\alpha$. Comparison between S9a-c shows that the nucleation sites are more concentrated in the higher clustering network. Also the frequency of IAs is higher in the more clustered case.

In Fig. S10 we show the effects of system size on the nucleation PDF. The sharpness of the nucleation sites remains

constant with system size and the number of nucleation sites is an extensive property of the system, giving rise to the same Lorenz curves when rescaled.

Inhibition

To check the effects of inhibition in the presence of nucleation sites, bursting and propagation we also created cultures where a 20% of the neurons was inhibitory and performed simulations with their connections active (E+I networks) and blocked (E networks). The results for a specific run can be seen in Fig. S11 where we show the nucleation PDF for the same network with inhibition blocked and active. In both cases we observe the same nucleation process but the specific locations of the nucleation sites have changed. The difference in the nucleation sites and their relative importance further emphasizes the relevance of the exact wiring in the nucleation process.

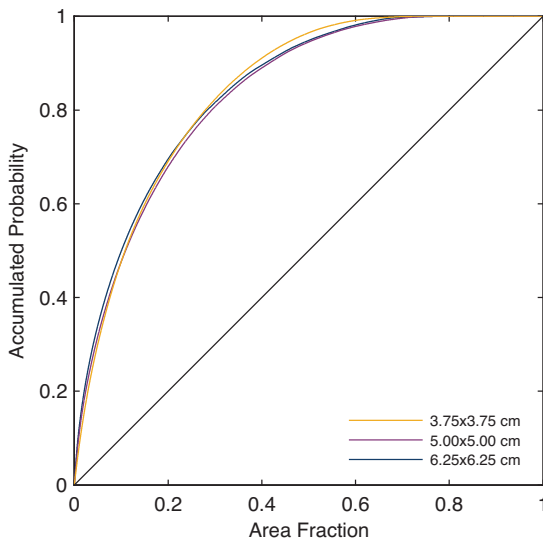


Fig. S10. Dependence of nucleation probability density with system size. Lorenz curves for the nucleation probability density for a network embedded in a square substrate with three different sizes. Each curve has been averaged over 10 different network realizations containing ~ 1000 bursts each. The shape of the probability density function scales with system size, but the number of nucleation sites is an extensive property of the system.

Regular graphs: Avalanches and nucleation in a toy model

Motivation. The avalanche dynamics studied in metric networks can be better understood by using a network toy model. In this model all neurons are topologically identical, i.e. all have the same pattern of connections, but the neuronal dynamics remains exactly the same as for the metric networks. This modeling strategy qualitatively identifies those aspects that are robust (i.e. independent of the network structure) and provides quantitative results regarding the relevance of the different triangular loops. The latter aspect is usually out of reach in full complex metric networks.

Network construction. We construct 4 main regular networks, labeled $M_0 - M_4$ which are characterized by having all the same number of neurons ($N = 200$) and the same connectivity degree ($k = 35$), but differing in the number of Feed-forward (FF) and Feed-back (FB) triangular loops.

The first step to construct each network is to obtain a full feed-forward network of N neurons with k output connections each ($3k < N$). This regular network is constructed using an iterative process to generate the adjacency matrix. For the first column, which corresponds to the output connections of the first neuron, the k -th connections are assigned sequentially in the clockwise (CW) direction, i.e. $A_{i1} = (0, 1, 1, \dots, 1^{(k+1)}, 0, \dots, 0^{(N)})$. The matrix entries for the following columns are then assigned by applying circular permutations to the first one, a process that is iteratively repeated until the whole matrix is spanned. We denote the resulting network configuration by $M_{k,0}$, meaning that k connections are assigned in the clockwise (CW) direction and 0 in the counterclockwise (CCW). To add feedback loops in the adjacency matrix, a combination of CW and CCW connections is needed: $A_{i1} = (0, 1, \dots, 1^{(\ell+1)}, 0, \dots, 0, 1^{(N-k+\ell+1)}, \dots, 1^{(N)})$ which corresponds to $M_{\ell,k-\ell}$ (ℓ CW connections, and $k - \ell$ CCW connections per neuron).

A good way to visualize the connectivity structure of these regular networks, is to consider that neurons are in a circle with a given number of connections to the right and a given number of connections to the left (Fig. S12a). A motif of connectivity can be defined as the structure of connections of each neuron. In our case, as illustrated Fig. S12a, we assign the same motif to all the neurons. A different motif assigned to the neuron leads to a different type of network with different numbers of FF and FB loops associated.

As indicated we have considered 4 different motifs (i.e. 4 main regular networks) M_0 is characterized by a motif where the connections project to the neighboring neurons only in the clock-wise direction. This is, in a sense, a fully asymmetric (one-sided) arrangement. The full symmetric motif would have the same number of clock-wise and anticlock-wise connections. We name this network as M_3 while introduce $M_1 - M_2$ for a general intermediate case with a non-symmetric arrangement. Notice that different motifs lead to different number of Feed-Forward and Feed-Back loops in the clustering structure of the network.

Results. We can study now the dependence of avalanche dynamics on the structure of the connectivity, i.e. the number and type of loops. As a first general result we observe the presence of both background and ignition avalanches, as in the metric network. Fig. S12b shows the distribution of Background Avalanches for the four regular networks. We also show the statistics for a random network, where we have switched connections between randomly selected neurons while keeping the connectivity degree of each neuron. The BA distributions for the four regular networks have a similar trend with a reasonable data collapse.

The IAs frequency is highly sensitive to the wiring of the network. This sensitivity becomes clear in Fig. S12c, where we show the IA frequency of the four regular networks and the random one. We note that the nucleation time (the inverse of the IA frequency) for the random network is two orders of magnitude higher than the regular ones. Such a difference is associated to the weaker correlations between neurons in the random network. For the regular cases, however, the difference is associated to the balance between FF and FB loops. Indeed, although a larger number of FF triangles initially favors nucleation, the shortest nucleation times are obtained when a finite amount of recurrence (FB loops) is introduced.

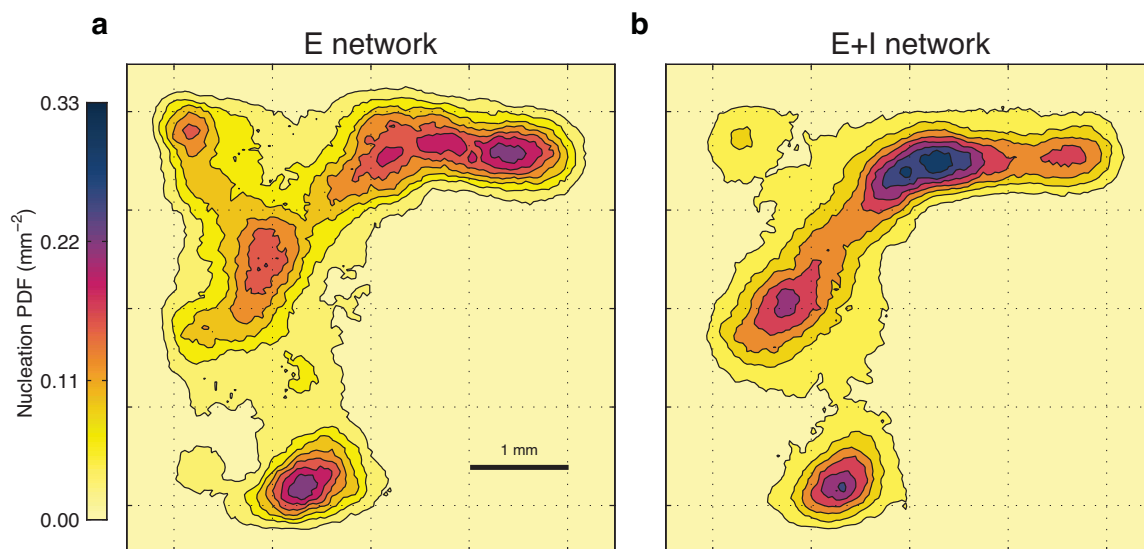


Fig. S11. Effects of inhibition in the nucleation sites. A network equivalent to the ones presented in the main text was generated with a 20% of neurons considered inhibitory. And synaptic strengths were set to $g_A = 13$ mV and $g_G = -26$ mV. For the E network case all gabaergic connections were blocked. **a**, Nucleation probability density map for the E network. **b**, Nucleation probability density map for the E+I network. The nucleation sites have moved respect to the E network case and their relative strength has also changed. These changes reflect the importance of the specific connectivity patterns in the emergence of the different nucleation sites.

For these particular networks, the optimal ratio of FF triangles to the total number of triangles is $R_{FF} \simeq 0.85$. As a reference we note that for an infinite random graph $R_{FF} = 0.75$. It is suggestive that the simulated, culture-like, *i.e.* metric, networks yield values close to the above optimum value, with $R_{FF} = 0.87$.

These results indicate that the general structure of avalanches followed by nucleation is a robust scenario and, more importantly, that random graphs would need a much larger time to nucleate once the network has recovered from synaptic depression. This indicates that the metric correlations in the connectivity generated by the growth process of axons leads to much faster nucleation. On the other hand, we can see that the detailed wiring at the level of triangles can introduce significant differences in the characteristic time scale of nucleation. This sensitivity of the IAs nucleation times to the detailed wiring explains why regions of similar average connectivity in the metric networks show significant differences in nucleation probability.

Theoretical analysis

Dynamical noise amplification. To gain quantitative insight, we may assume for simplicity that the noise in each neuron takes the form of a Poisson shot process with frequency λ and that the input from a firing neuron just adds another shot of the same amplitude. The neuron fires whenever it accumulates at least m shots in a time window Δt . Under these assumptions the probability p_m of firing if it receives m inputs from other neurons reads

$$p_m = e^{-\lambda\Delta t} \sum_{i=m_0-m}^{\infty} \frac{(\lambda\Delta t)^i}{i!} = \mathcal{P}(m_0 - m, \lambda\Delta t), \quad [13]$$

where $\mathcal{P}(m_0 - m, \lambda\Delta t)$ is the regularized gamma function, a monotonically non-decreasing function of m , that is increasing from the value p_0 that sets the spontaneous firing rate, $\omega_0 \sim p_0/\Delta t$, to $p_m = 1$ for $m = m_0$ (see Fig.6a of the manuscript). For $m' > m_0$ the analytical continuation of this function to negative integer values of its first argument yields the correct values $p_{m'} = 1$. $\mathcal{P}(m_0 - m, \lambda\Delta t)$ quantifies in this simplified model how the probability of induced (sub-quorum) firing is enhanced by inputs from other firings. The maximum sensitivity of the firing probability to the addition of a single input occurs for $\epsilon \equiv \lambda\Delta t/(m_0 - 1) \sim 1$. The parameter ϵ is an appropriate measure of the noise intensity, and will typically be smaller than 1.

If we quantify the importance of sub-quorum firing in terms of the quorum fraction $f(p_c) = m_0^*/m_0$, as the required number of inputs m_0^* that gives a firing probability of p_c , that is, by the implicit equation

$$\mathcal{P}(m_0 - m_0^*, \lambda\Delta t) = p_c, \quad [14]$$

then for sufficiently large m_0 , $\mathcal{P}(m_0 - m, \lambda\Delta t)$ has a narrow sigmoidal shape with fast variation between 0 and 1 centered around $m_0^* \simeq (1 - \epsilon)m_0$ (see Fig.6a of the manuscript). Specifically, one can show that

$$\lim_{m_0 \rightarrow \infty} \mathcal{P}(m_0(1 - \eta), \epsilon(m_0 - 1)) = \Theta(\eta - (1 - \epsilon)), \quad [15]$$

where Θ is the Heaviside step function. Therefore, for large m_0 one may unambiguously define an effective quorum fraction $f^* = 1 - \epsilon$, such that for $m < m_0 f^*$ the firing probability is $p_m \simeq 0$ while for $m > m_0 f^*$ it is $p_m \simeq 1$.

Topological noise amplification. To pursue the influence of the network wiring in the amplification of the firing probability we can compute the effect of a feed forward motive as that depicted in Fig.6b of the manuscript, where n neurons A_1, \dots, A_n

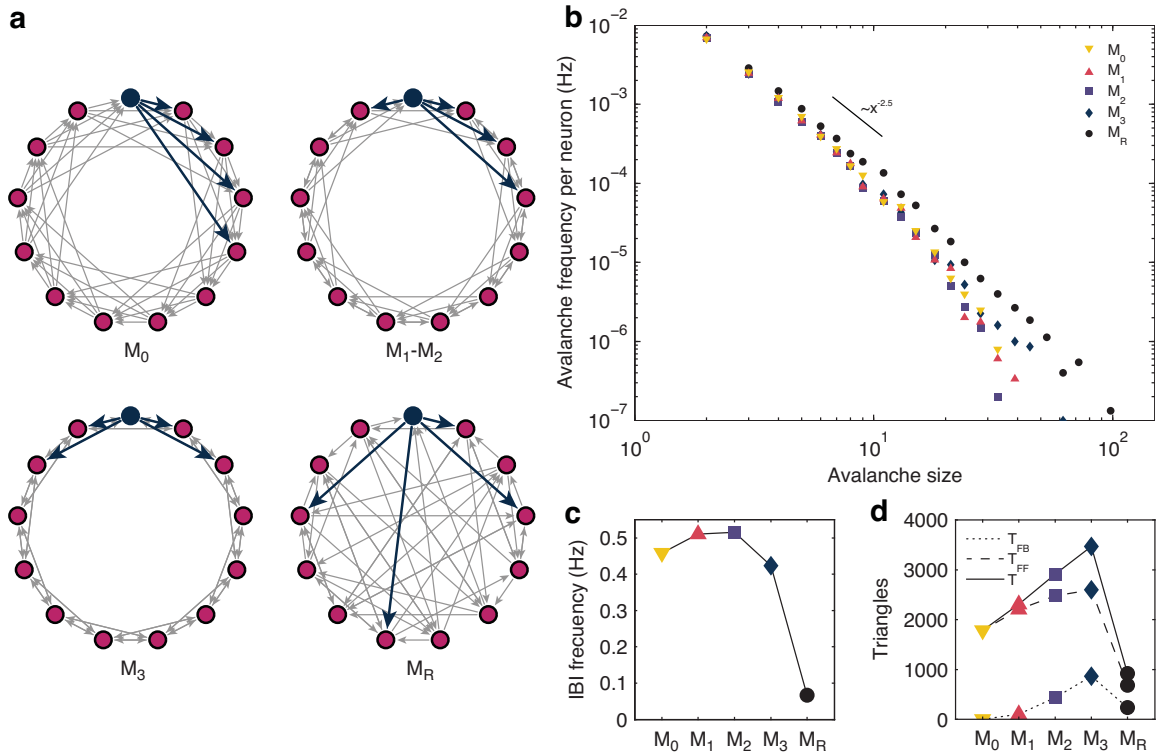


Fig. S12. Statistics of Background Avalanches (BA) for regular, non-metric networks. **a**, 4 examples of regular networks, with four connections per neuron (the motif in dark color is repeated for all 13 neurons). M_0 designates the case with fully asymmetric (one-sided) connections, while M_3 designates the fully symmetric arrangement. The case depicted as $M_1 - M_2$ describes a generic intermediate case with a non-symmetric arrangement. These network configurations provide scenarios with a different balance between FF and FB triangular loops, with only FFs in M_0 and the maximum number of FBs in M_3 , and while keeping the number of input and output connections constant. Finally, M_R designates a random case with the same number of connections per neuron. **b**, Avalanche frequency as a function of the avalanche size for regular networks of 200 neurons, 35 connections per neuron, and different motif arrangements, including: asymmetric $M_0 = (35, 0)$, two intermediate cases $M_1 = (30, 5)$ and $M_2 = (25, 10)$, symmetric $M_3 = (18, 17)$, and random M_R . The values in brackets denote the number of clockwise connections and counterclockwise connections. The dashed horizontal lines correspond to the frequency of IA for the four regular networks (values indistinguishable in this scale) and the random one. The dashed line marks the crossover scale for departure from the power law behavior, with approximate slope $-5/2$. **c**, Nucleation frequency for the different regular and random networks, showing a non-monotonic behavior. **d**, Statistics of FFs, FBs and total number of triangles for the different networks.

are connected directly to a neuron C , and indirectly through a set of n' intermediate neurons $B_1, \dots, B_{n'}$, forming n' independent feed-forward loops between A and C . If there are no other connections, the firing probability of C $p_{nn'}$ if the set A_i fires together within a Δt can be expressed as

$$p_{nn'} = \sum_{k=0}^{n'} \binom{n'}{k} p_n^k (1 - p_n)^{n'-k} p_{k+n}. \quad [16]$$

This 'dressed' probability of induced firing is significantly larger than the 'bare' induced probability p_n . In particular, one may compute the dressed critical fraction $f_{n'}(p_c)$, as the quorum fraction in the presence of n' feed-forward loops, and see that this drops monotonically with n' , with the fastest decay for small n' , as shown in Fig.6b of the manuscript. The extension to more complex wiring must be explored numerically. In the section on regular graphs above we have illustrated the complexity of the topological amplification obtaining the nucleation time for relatively simple networks.

Quorum percolation analysis

As a reference in the theoretical analysis we may estimate the probability of nucleation from a pure percolation analysis, using the ideas of quorum percolation [2, 16], that generalize the idea of percolation to the case where a minimum quorum of m inputs is required for a neuron to fire. By keeping the connectivity correlations of the metric network, but neglecting the dynamic correlations between neuron firings, this analysis would reduce the probability of percolation of the entire network to having a minimum number of simultaneous spontaneous firing (the critical fraction) within a spatially correlated area, sufficiently large so that metric correlations would then propagate percolation to the entire system. Within a correlated area, the network is essentially a (finite) random graph of N_c neurons, with a critical percolation fraction of the order of $m_0/\langle k \rangle$ or larger, so the number of spontaneous firings that must occur within a Δt in that area must be $n_c \sim N_c m_0 / \langle k \rangle$ or more. A conservative estimate of the probability of percolation induced by spontaneous firing of frequency ω_0 of a nucleus with N_c neurons would scale as $P_{perc} \sim \mathcal{P}(n_c, N_c \omega_0 \Delta t) \sim \exp(-N_c \omega_0 \Delta t) (N_c \omega_0 \Delta t)^{n_c} / n_c!$. For typical values in experiments and simulations this estima-

tion is off by many orders of magnitude, because of the strong dependence on the small parameter $\omega_0 \Delta t$. For a typical example of our simulated cultures, we find that a minimum number of $n_c \sim 20$ neurons must be excited out of the $N_c \sim 85$ contained in a circle of radius 0.3mm. With $\omega_0 \sim 0.4\text{Hz}$ and $\Delta t \sim 20\text{ms}$ we have $P_{perc} \sim 10^{-23}$. These extreme values cannot be brought significantly close to realistic ones values by replacing the quorum m_0 and the firing frequency ω_0 by some renormalized values along the lines discussed above. The failure of the percolation estimate dramatically illustrates the importance of dynamic correlations of the neuron firing, that manifest in the form of avalanches. Within our dynamical scenario, the critical event is the occurrence of an IA, that is, an avalanche that excites the local critical percolation fraction. As discussed in the main text, the probability of such an event is much larger, not only because big avalanches occur relatively often, but also because the area that contributes to the formation of such avalanches is much larger than the nucleation sites, where they project the activity.

Model parameters

The table below lists all parameters used in the model together with their numeric range.

Parameters	Value
System-wide parameters	
System size $L \times L$	$L = 5 - 20 \text{ mm}$
Density	$\rho = 10^2 - 10^3 \text{ neu/mm}^2$
Morphological parameters	
Soma size (fixed)	$r_a = 7.5 \mu\text{m}$
Dendritic tree (Gaussian pdf)	$\mu = 150 \mu\text{m}, \sigma = 20 \mu\text{m}$
Axonal length (Rayleigh pdf)	$\sigma = 800 \mu\text{m}$
Axonal segment length (fixed)	$l_s = 10 \mu\text{m}$
Axonal segment angle (G. pdf)	$\mu = 0, \sigma = 0.1 \text{ rad}$
Soma parameters	
Resting membrane potential	$v_r = -60 \text{ mV}$
Threshold membrane potential	$v_t = -45 \text{ mV}$
Peak membrane potential	$v_p = 35 \text{ mV}$
Reset membrane potential	$v_c = -50 \text{ mV}$
	$\tau_c = 50 \text{ ms}$
	$k = 0.5 \text{ mV}^{-1}$
	$\tau_a = 50 \text{ ms}$
	$b = 0.5$
	$d = 50 \text{ mV}$
Synapse parameters	
Depression recovery time	$\tau_D = 5 \cdot 10^2 - 2 \cdot 10^4 \text{ ms}$
Depression decay	$\beta = 0.8$
AMPA current strength	$g_A = 10 - 50 \text{ mV}$
AMPA current decay time	$\tau_A = 10 \text{ ms}$
GABA _A current strength	$g_G = 20 - 100 \text{ mV}$
GABA _A current decay time	$\tau_G = 20 \text{ ms}$
Noise parameters	
White noise strength	$g_s = 3 \cdot 10^2 \text{ mV}^2 \text{ ms}$
White noise auto-correlation	$\langle \eta(t)\eta(t') \rangle = 2g_s \delta(t - t')$
Shot noise frequency	$\lambda = 0.01 - 0.05 \text{ ms}^{-1}$
Shot noise strength (minis)	$g_m = 10 - 50 \text{ mV}$
Shot noise decay time	$\tau_m = \tau_A$
Simulation parameters	
Algorithm	2nd order Runge-Kutta
Time step	$\Delta t = 0.01 \text{ ms}$
Typical Run time	10^4 s

Additional Files

Movie 1: activity-cultures.avi. Spontaneous activity recorded simultaneously in two mini-cultures, 3 mm in diameter each and separated by 1 mm. The experiment was recorded at 83.33 frames per second (fps) with both excitation and inhibition active, at DIV 8. Movie is played at 3X real time. The total duration of the movie corresponds to 3.5 min of actual recording. The movie illustrates the rich spontaneous activity of the cultures and our ability to record various cultures simultaneously.

Movie 2: front-mini.avi. Spontaneous front propagating in a quasi-rectangular mini-culture of $7 \times 3 \text{ mm}^2$ in size, at DIV 11. The experiment was recorded at 33 fps with inhibition blocked. Front starts at the right edge and advances at 25 mm/s towards the left. Movie is played at 1/3 real time for a better visualization of the advance of the front. The total duration of the movie corresponds to 3 s of real measurement.

Movie 3: front-big.avi. Spontaneous front propagating in a 13 mm diameter culture, with activity recorded in an area of $4.2 \times 3.2 \text{ mm}^2$, at DIV 9. The experiment was recorded at 33 fps with inhibition blocked. Front starts at the bottom-center and advances upwards at 20 mm/s. Movie is played at 1/3 real time for clarity. The total duration of the movie corresponds to 1.5 s of real measurement.

Movie 4: burst-simulation.avi. Movie showing 4 consecutive bursts without the inter burst period for the simulations from Fig. 5 in the main text. Color code represents fluorescence intensity based on Ca^{2+} concentration. Ca^{2+} on each neuron is calculated from

$$\frac{d}{dt}[\text{Ca}^{2+}](t) = -\frac{1}{\tau_{\text{Ca}}}[\text{Ca}^{2+}](t) + A_{\text{Ca}}\delta(t - t_s), \quad [17]$$

where τ_{Ca} is the decay time constant from the Ca^{2+} signal, A_{Ca} the increase in Ca^{2+} after each spike and t_s the time of a spike. Then the fluorescence intensity of each neuron is obtained from

$$F(t) = \frac{[\text{Ca}^{2+}](t)}{[\text{Ca}^{2+}](t) + K_d}, \quad [18]$$

where K_d is a constant associated to the saturation of the signal.

Movie 5: preburst-simulation.avi. Movie detailing the exact structure of an IA. Color is associated to the activation time of each neuron during the Ignition Avalanche. In the rate panel the neurons are ordered in the unit circle based on their first time of activation. The explosion of activity around $\sim 100 \text{ ms}$ can clearly be seen in this representation. This IA belongs to a network with low density $\rho = 100 \text{ neurons/mm}^2$ and maximum connection probability $\alpha = 1$ to allow a better visualization of its structure.

Movie 6: avalanches.avi. Movie showing all activity before a burst for a network equivalent to the one shown in Fig. 5 from the main manuscript. Background Avalanches (both spikes and participating connections) are shown each with a different color, and only the spikes corresponding to the last 20 ms of each avalanche are shown for a given time frame. The Ignition Avalanche associated to the burst is shown in white, and when the ignition activity begins to saturate the drawing of the connections is omitted.

1. Segal, M. and Manor, D. Confocal microscopic imaging of $[Ca^{2+}]_i$ in cultured rat hippocampal neurons following exposure to N-methyl-D-aspartate. *J. Physiol.* **448**, 655–676 March (1992).
2. Soriano, J., Rodríguez Martínez, M., Tlusty, T., and Moses, E. Development of input connections in neural cultures. *Proc. Natl. Acad. Sci. U.S.A.* **105**(37), 13758–13763 September (2008).
3. Wagenaar, D. A., Pine, J., and Potter, S. M. An extremely rich repertoire of bursting patterns during the development of cortical cultures. *BMC Neurosci.* **7**, 11 (2006).
4. Wen, Q., Stepanyants, A., Elston, G. N., Grosberg, A. Y., and Chklovskii, D. B. Maximization of the connectivity repertoire as a statistical principle governing the shapes of dendritic arbors. *Proc. Natl. Acad. Sci. U.S.A.* **106**(30), 12536–12541 July (2009).
5. Izhikevich, E. M. Simple model of spiking neurons. *IEEE Trans. Neural Netw. (1990-2011)* **14**(6), 1569–1572 (2003).
6. Alvarez-Lacalle, E. and Moses, E. Slow and fast pulses in 1-D cultures of excitatory neurons. *J. Comput. Neurosci.* **26**(3), 475–493 June (2009).
7. Golomb, D. and Amitai, Y. Propagating neuronal discharges in neocortical slices: computational and experimental study. *J. Neurophysiol.* **78**(3), 1199–1211 September (1997).
8. Tsodyks, M. V. and Markram, H. The neural code between neocortical pyramidal neurons depends on neurotransmitter release probability. *Proc. Natl. Acad. Sci. U.S.A.* **94**(2), 719–723 January (1997).
9. Tsodyks, M., Uziel, A., and Markram, H. Synchrony generation in recurrent networks with frequency-dependent synapses. *J. Neurosci.* **20**(1), RC50 January (2000).
10. Garcia-Perez, E., Lo, D. C., and Wesseling, J. F. Kinetic isolation of a slowly recovering component of short-term depression during exhaustive use at excitatory hippocampal synapses. *J. Neurophysiol.* **100**(2), 781–795 August (2008).
11. Cohen, D. and Segal, M. Network bursts in hippocampal microcultures are terminated by exhaustion of vesicle pools. *J. Neurophysiol.* **106**(5), 2314–2321 November (2011).
12. Cohen, D. and Segal, M. Homeostatic presynaptic suppression of neuronal network bursts. *J. Neurophysiol.* **101**(4), 2077–2088 April (2009).
13. Fagiolo, G. Clustering in complex directed networks. *Phys. Rev. E Stat. Nonlin. Soft Matter Phys.* **76**(2), 26107 August (2007).
14. Ahnert, S. E. and Fink, T. M. A. Clustering signatures classify directed networks. *Phys. Rev. E Stat. Nonlin. Soft Matter Phys.* **78**(3), 36112 September (2008).
15. Serrano, M. A. and Boguñá, M. Clustering in complex networks. I. General formalism. *Phys. Rev. E Stat. Nonlin. Soft Matter Phys.* **74**(5 Pt 2), 056114 November (2006).
16. Cohen, O., Keselman, A., Moses, E., Rodríguez Martínez, M., Soriano, J., and Tlusty, T. Quorum percolation in living neural networks. *Europhys. Lett.* **89**(1), 18008 January (2010).